DOI: https://doi.org/10.14311/TPFM.2020.022

LAMINAR-TURBULENT TRANSITION IN VIEW OF FLOW SEPARATION FROM ISOTHERMAL AND HEATED CYLINDER

J. Pech

Institute of Thermomechanics of the CAS, Dolejškova 1402/5, 182 00 Praha 8, Czech Republic

Abstract

This work presents insight to the laminar-turbulent transition in flow around cylinder through a numerical simulation, both in isothermal and heated case. The flow is modelled directly as a solution to the Navier-Stokes and Navier-Stokes-Fourier system. Reynolds numbers are considered in range 100-20000, ratio of cylinder-wall and upstream temperature is up to 1.5. Curves representing evolution of separation positions in time provide novel insight to vortex formation. Various regimes are recognized and some of them can be assigned to phenomenons described formerly in experiment.

Keywords: transition to turbulence, heated flow, cylinder flow, separation angle, Navier-Stokes-Fourier, spectral/hp element method.

1 Introduction

The theme of flow around cylinder is frequently revisited both in experiments and computations. Its geometry is simple, but the problem includes wide variety of generally observed phenomenons which are not fully understood so far. Presented results contribute to regime of transition to turbulence in unusual analysis of temporal evolution of flow separation points.

We assume the fluid as incompressible and study both isothermal case, when the temperature of the cylinder wall T_W is equal to the temperature of incoming fluid T_∞, and the case $T_W > T_\infty$. Change of temperature causes variation of fluid's material properties (density $\rho = \rho(T)$, dynamic viscosity $\mu = \mu(T)$, thermal conductivity $\kappa = \kappa(T)$, specific heat c_p is assumed constant) and accordingly local Reynolds number. Influence of heating to the flow was already studied in view of change in Strouhal number ([8], [7]), but the frequency of vortex shedding do not show the qualitative changes in flow structures, what was recognised from insight to evolution of separation points in the present study.

2 Mathematical model

We consider both isothermal and heated flow of incompressible fluid. For the isothermal case, we solve the Incompressible Navier-Stokes equations

$$\frac{\partial \mathbf{v}}{\partial t} + \mathbf{v} \cdot \nabla \mathbf{v} = -\nabla p + \frac{1}{\mathrm{Re}} \nabla^2 \mathbf{v} \tag{1a}$$

$$\nabla \cdot \mathbf{v} \tag{1b}$$

For the heated case, we assume the fluid to be calorically perfect, Newtonian and obeying Fourier law for heat flux. Mathematical model of the heated fluid then forms the Navier-Stokes-Fourier system with variable coefficients, which consists of balance of momentum, mass and energy

$$\rho \left(\frac{\partial \mathbf{v}}{\partial t} + \mathbf{v} \cdot \nabla \mathbf{v} \right) = -\nabla p + \frac{1}{\mathrm{Re}} \nabla \cdot (2\mu \mathbb{S}) + \frac{1}{\mathrm{Fr}^2} \rho \mathbf{g} \tag{2a}$$

$$\frac{\partial \rho}{\partial t} + \nabla \cdot (\rho \mathbf{v}) = 0 \tag{2b}$$

$$\rho \left(\frac{\partial T}{\partial t} + \mathbf{v} \cdot \nabla T \right) = \frac{1}{\mathrm{Re}\,\mathrm{Pr}} \nabla \cdot (\kappa \nabla T) + \frac{\mathrm{Ec}}{\mathrm{Re}} 2\mu \mathbb{S} : \mathbb{S}\,, \tag{2c}$$

where

$$\mathbb{S} = \mathbb{D} - \frac{1}{3}(\nabla \cdot \mathbf{v})\,\mathbb{I} \tag{3}$$

denotes the deviatoric part of the stress tensor (pure shear stress) and $\mathbb{D} = \frac{1}{2}\left[\nabla\mathbf{v} + (\nabla\mathbf{v})^{\mathrm{T}}\right]$. In (2c), term

$$\mathbb{S} : \mathbb{S} = \mathbb{D} : \mathbb{D} - \frac{1}{3}(\nabla \cdot \mathbf{v})^2 \tag{4}$$

models the effect of viscous heating[1] and the term $\frac{1}{\mathrm{Fr}^2}\rho\mathbf{g}$ models buoyancy[2]. The flow regime is characterized by dimensionless numbers in (2), Reynolds number $\mathrm{Re} = \frac{\rho^+_\infty |\mathbf{v}^+_\infty| L^+}{\mu^+_\infty}$, Froude number $\mathrm{Fr} = \frac{|\mathbf{v}^+_\infty|}{\sqrt{g^+_\infty L^+}}$ Prandtl number $\mathrm{Pr} = \frac{c^+_{p\,\infty}\mu^+_\infty}{\kappa^+_\infty}$ and Eckert number $\mathrm{Ec} = \frac{|\mathbf{v}^+_\infty|^2}{c^+_{p\infty} T^+_\infty}$. We use superscript "+" for quantities with physical dimensions and subscript "$_\infty$" for fixed upstream/farfield values, g^+_∞ is gravitational acceleration and L^+ is a characteristic length (cylinder diameter).

3 Numerical method

Numerical approximation in spatial coordinates is based on spectral/hp element method [3]. Discretisation in time follows semi-implicit approach based on idea proposed in [4] for isothermal case and [5] for the heated case[3].

The spectral/hp element method (SEM) combines accuracy and efficiency of the spectral method with capability of general geometry approximation known from the low order finite elements. The spectral elements Ω^e, whose count is E, are conforming and cover the computational domain $\Omega = \cup_{e=1}^{E}\Omega^e$, while locally, on each element, an approximated function is expanded over a rich (here 2D) basis $\mathcal{B}_N = \{\phi_{pq}\}_{p,q=0}^{N}$

$$u(x,y) \approx \sum_{e=1}^{E}\sum_{p,q=0}^{N} \hat{u}^e_{pq}\phi_{pq}(x,y)\,. \tag{5}$$

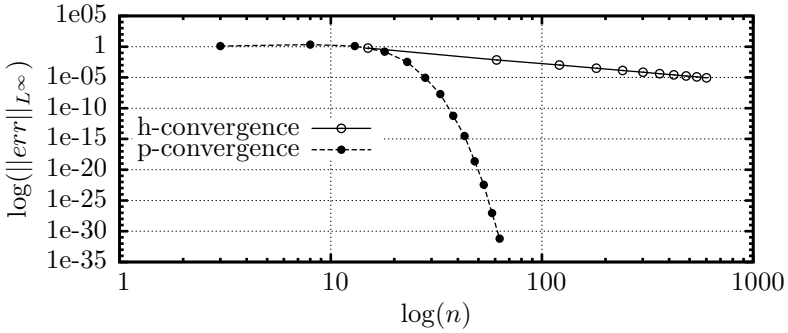

Figure 1: Comparison of high and low order convergence of approximation error, "err", on 1D smooth function. Spectral "p-convergence" for single element ($E = 1$, $n = N$) vs. algebraic "h-convergence" for linear approximation ($N = 1$, $n = E + 1$). Quad-precision arithmetic was used in this illustration.

[1] Viscous heating do not have distinguishable influence to the flow structures in studied regimes, but in the isothermal case resulting temperature field shows distribution of energy losses due to viscous dissipation.

[2] Influence of buoyancy was not explicitly studied and was included for completeness as it is computationally cheap. The flow is in regime of forced convection, but buoyancy has a comparable influence to the solution as the viscous term (e.g. for $T_W/T_\infty = 1.5$ and $\mathrm{Re} = 600$ $\frac{1}{\mathrm{Re}} \approx \frac{1}{\mathrm{Fr}^2}$)

[3] In [5], system (2) is simplified to constant density in energy equation (2c), while here the density is variable also in the energy equation.

Hierarchical basis, $\mathcal{B}_N \subset \mathcal{B}_{N+1}$, is used in present simulations. $(N+1)^2$ is the number of modes in the basis over each element Ω^e and N is the highest degree polynomial used in the basis in each coordinate direction. In case of quadrilateral elements, $\mathcal{B}_N$ is generated as the tensor product of two 1D basis, $\phi_{pq}(x,y) = \phi_p(x)\phi_q(y)$. On triangles, a modification is needed, but the basis is also generated as the tensor product, see [3].

The approximation error converges accordingly to decay of expansion coefficients ($\hat{u}_{pq}$), while these converge exponentially (p-convergence) if a smooth function is approximated. This is in contrast to low order methods converging by refinement of computational mesh (h-convergence), c.f. Figure 1. Fast decay in spectra results in relatively low number of degrees of freedom in the algebraic system.

The sum of highest coefficients of element-boundary expansions, e.g. for quadrilateral element

$$S^e(u) = \hat{u}^e_{0N} + \hat{u}^e_{0(N-1)} + \hat{u}^e_{1N} + \hat{u}^e_{1(N-1)} + \hat{u}^e_{N0} + \hat{u}^e_{(N-1)0} + \hat{u}^e_{N1} + \hat{u}^e_{(N-1)1}\,, \tag{6}$$

can be used for a direct estimate of spatial approximation quality. The pointwise error between the exact function and its approximation *is not smaller than* S^e and we can easily detect elements, where the function is not approximated to desired accuracy in spatial coordinates. This approach is shown in Figures 2 and 3, where the expansion over quadrilateral elements with $N = 24$ is shown for a function well resolving boundary layer.

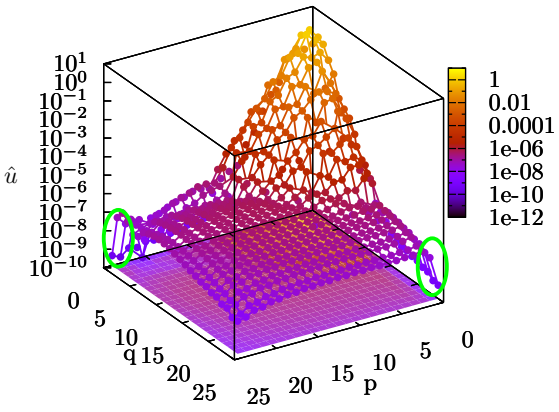

Figure 2: Expansion spectrum $\hat{u}_{pq}$ of x-component of velocity, on one of the elements in quadrilateral mesh (element no. 25 highlighted in Figure 3). Coefficients summed for error estimate in $S^{25}(u)$ are highlighted in green ellipses ($S^{25}(u) = 1.3 \times 10^{-7}$).

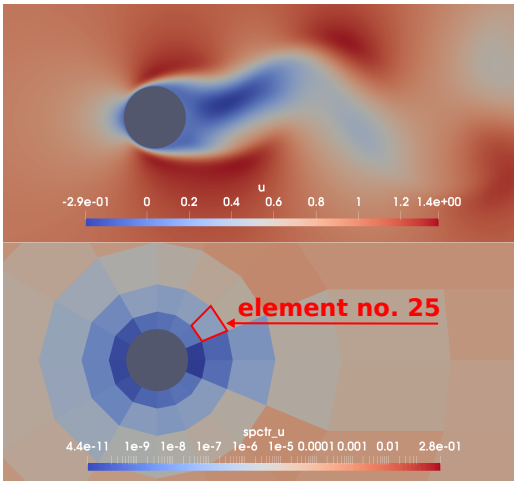

Figure 3: Detail to cylinder area. x-component of velocity u (top). Logarithmic colouring of highest boundary modes sum S^e, reflecting quality of spatial approximation of function u (bottom). Note, that minimal values of $S^e \approx 10^{-11}$ are in elements neighbouring to the cylinder surface.

Discretisation in time is based on Backward difference formula with consistent extrapolation. The equation system is finally decoupled to 4 equations of type

$$(\nabla^2 - \lambda)u = f_u\,. \tag{7}$$

These are discretized over spectral/hp element spaces and solved within separated algebraic systems. An important role plays the high order pressure boundary condition which is in the heated case an extension (presented in [5]) of idea proposed in [4].

The scheme was implemented within the Nektar++ framework ([1]), an open source library with support for spectral/hp element method.

We do not impose any restrictions to the form of temperature dependencies of material parameters μ, ρ and κ. The power-law fit, $f(T) = \dfrac{f^+_{ref}}{f^+_\infty}\left(\dfrac{T^+}{T^+_{ref}}\right)^{\omega_f}$, through tabulated data was chosen.

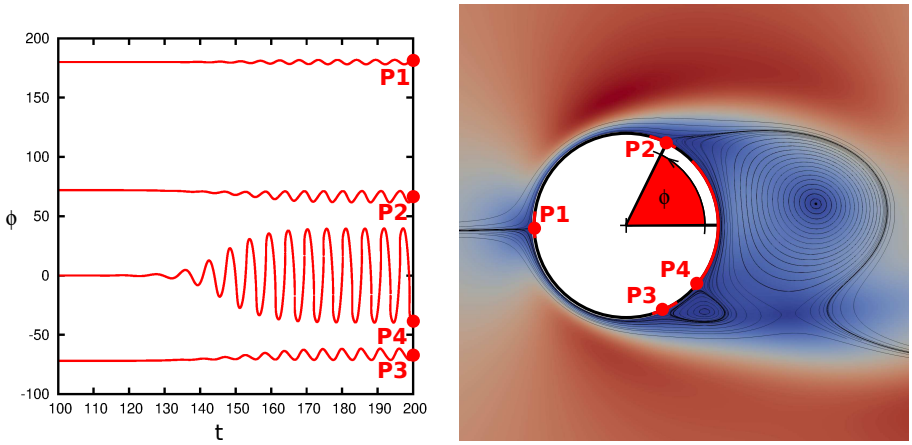

Figure 4: Evolution of detected "separation" points in time and definition of the angle ϕ, which is measured from the downstream extremal point of the cylinder. All the data belong to Re = 160.3, quadrilateral mesh $N = 25$.

Particular constants for air at $T^+_{ref} = 285\text{K}$ are

$$\mu_{ref} = 1.78 \times 10^{-5}\text{Pa.s}\,, \rho^+_{ref} = 1.24\text{kg.m}^{-3}\,, \kappa^+_{ref} = 0.025\text{W.m}^{-1}\text{.K}^{-1}$$

$$\omega_\kappa = 0.84\,, \omega_\rho = -1.0013\,, \omega_\mu = 0.72$$

Scheme of order 2 in time was used in all presented simulations. Computational domain for lower Re was decomposed into 2360 triangular elements and had extent 150×100 with unitary cylinder diameter. Cylinder boundary was formed by 12 elements. Curves approximating the cylinder surface and half-circular inlet boundary were represented by 15 Gauss-Legendre-Lobatto (quadrature) points. A competitive computation was done with extended domain extent (500x500 cylinder diameters), quadrilateral mesh consisting of 289 elements only, but relatively high polynomial degree ($N = 24$).

4 Results

Outputs of present calculations were compared with experiments discussed in [2], where categorisation of flow structures is provided for isothermal case within a sufficiently wide range of Reynolds numbers.

We evaluate quantity

$$\frac{\partial \mathbf{v}}{\partial \mathbf{n}} \cdot \mathbf{t} \tag{8}$$

pointwise over the cylinder surface in elemental grid/quadrature points. The separation is detected, if (8) is equal to zero. All functions are evaluated in quadrature points of elements, but these points are far from each other in central parts of high order elements in comparison to element sizes of low order methods. Therefore we interpolate linearly to increase accuracy of the separation angle position. Example of temporal evolution of detected angles (ϕ) and its visualization for a particular time is in Figure 4, where we also introduce notation of significant separation positions referenced later in the text.

Higher accuracy in spatial coordinates causes later onset of wake oscillation (observable around $t > 120$ in Figure 4, c.f. [6]). For $47 \lesssim \text{Re}$ evolution of positions P1-P4 exhibit periodic motion, which can be described as a functional dependence on time. In contrast to time evolution of positions P2 and P3, which resemble sine function, evolution of point 4 bends remarkably with increasing Re also in lower range of $47 \lesssim \text{Re} \lesssim 140$. For higher Re, P4-curve degenerates and becomes nonunique during a part of the period, see Figure 5.

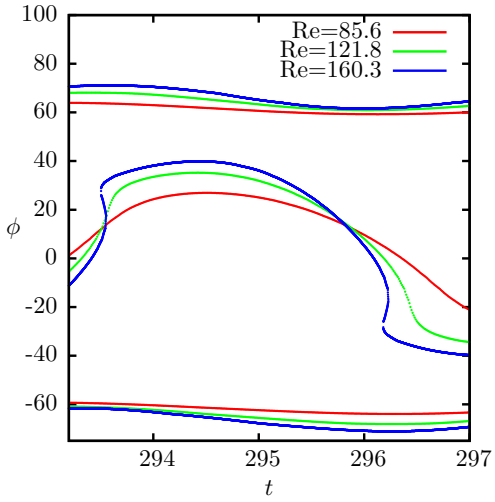

Figure 5: Degeneration of unique function describing position "P4" (Re = 85.6, Re = 121.8) to nonunique-in-time curve (Re = 160.3) with increasing Re (point P1 is here ommited).

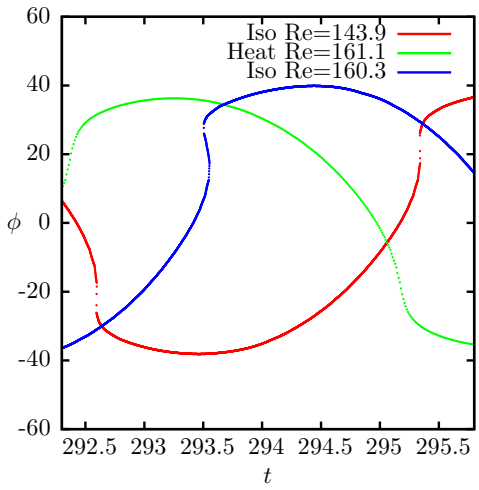

Figure 6: Comparison of cylinder heating ("Heat"..$\tilde{T}$ = 1.5, "Iso"..isothermal) influence to transitional regime. Detail view to position P4.

Nonuniqueness implies, that there coexist more than 4 separation points. This can be seen for Re = 160.3 in Fig. 5), where 6 points are detected for $t \approx 293.5$ and $t \approx 296.2$. The critical Reynolds number for this effect lies around $\mathrm{Re}_c \approx 143.8$, as follows from our simulations (see Figure 6). The second interpretation is, that within the amplitude range for P4, new separation poins emerge, alternately above and under the cylinder's horizontal axis of symmetry. The new separation points emerge in pairs and travel over the cylinder surface in mutually opposite directions. Finally, one of these new points merges with the old one while both disappear. Regarding the vortex structures, existence of the new pair of separation points indicate formation of a new secondary vortex. Disappearance of one new and the old one indicate, that the new secondary vortex merged with stronger primary one and this structure sheds from the cylinder surface. It should be emphasized, that phenomenon of the new emerging separations very well coincides with appearance of second-order instability (also called "transitional waves") observed in experiments, see e.g. [2]. The same critical Reynolds number is connected with instability in cylinder-spanwise direction and onset of 3D vortical structures. Sinusoidal evolution of frontal point (P1) was observed for all studied regimes and its temporal evolution coincides with evolution of lift coefficient, however, the change in character of vortex shedding was not recognized in evolution of integral type quantities as is drag or lift coefficient.

Influence of cylinder wall heating to periodic patterns in separation points data was observed. In Figure 6, we can see that the case Re $\approx$ 160, which is safely above the transition to regime with secondary instability, suppresses the instability if the cylinder is heated, curve describing position P4 becomes a unique function in this case. Generally, we can conclude, that if parameters of air are used in the solution, the flow adopts structures similar to lower Re accordingly to ratio of cylinder wall T_W and inlet T_∞ temperatures ($\tilde{T} = T_W/T_\infty = 1.5$ in Figure 6). This observation is also in a good agreement with concept of the effective Reynolds number ([8]). We can conclude, that for $\tilde{T} = 1.5$ the onset of secondary structures was observed around Re = 161.

Both spatial and temporal gradients of solution change rapidly with increasing Re. $N = 9$ and $\Delta t = 0.001$ was used in above mentioned simulations, but a higher polynomial degree was needed and Δt had to be shortened accordingly for higher values of Re (mesh fixed). Insufficient spatial resolution causes erroneous detections of separation points, c.f. Figure 7 since points of inter-element connections on the cylinder ensure only $\mathcal{C}^0$ continuity and (8) evaluates velocity gradients which accumulate numerical error toward element boundaries. Difference in solution and solver instability occurs for too long timesteps.

Accuracy of this kind of computations has to be checked carefully, because numerical oscillations

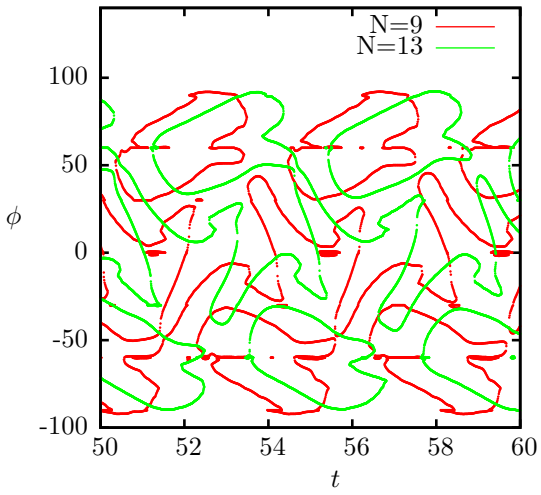

Figure 7: Wrong detections of separation points as a result of insufficient spatial approximation. Pattern for Re = 1400.

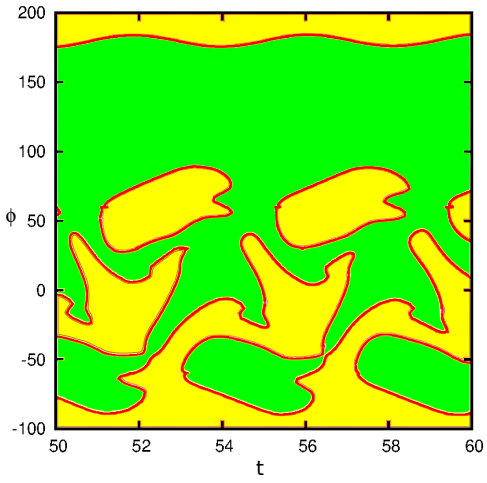

Figure 8: Evolution of separation angles with highlighted areas of positive/clockwise (green) and negative (yellow) rotation of vortices (Re = 1200, $N = 13$).

may be mistakenly interpreted as separation points or turbulent structure. In present simulations, analysis of spectra (see Fig. 3 and description) was used as functional space independent indicator of achieved accuracy.

For sufficiently resolved cases, when spurious detections were suppressed, we observed increasing number of detections with increasing Re, e.g. 14 for Re = 2000 or 88 for Re = 20000.

While increasing Re above the critical value for the secondary instability, the P4 curve bends progressively, but structure of P2-P4 do not change substantially. Character of shedding changes again between Re = 300 and Re = 400 where new separations occur, this time at positions P2 and P3. With this transition, the oscillation ranges of pairs P2, P4 and P3, P4 start to overlap, but the curves stay separate.

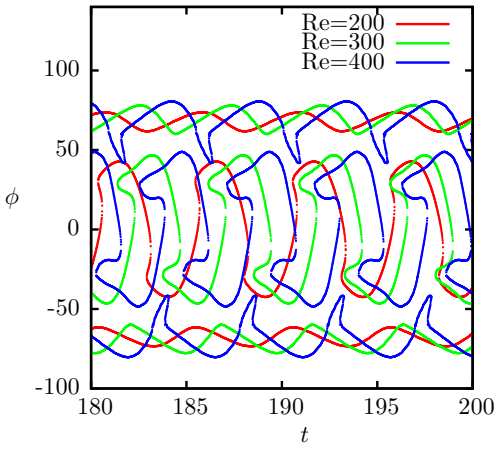

Figure 9: Temporal evolution of separation points (omitting point "P1") for Re $\in \{200, 300, 400\}$.

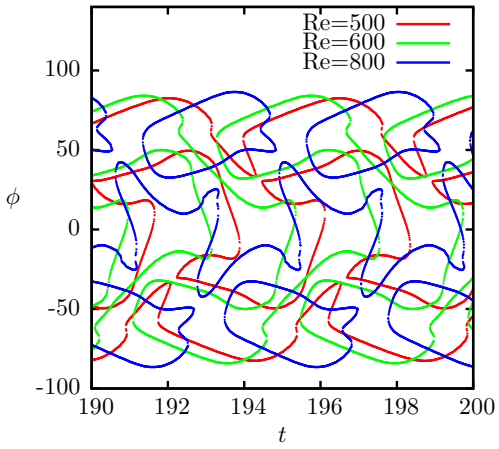

Figure 10: Temporal evolution of separation points (omitting point "P1") for Re $\in \{500, 600, 800\}$.

Heating of the wall changes the material properties and lowers the local Reynolds number in

the case of flow of air. Accordingly, the separation curves exhibit similarity to isothermal case with lower Re, c.f. Figure 11. Roughly estimated from curve shapes in available data, heating $\tilde{T} = 1.5$ lowers Re by ≈ 60 in range $100 \leq \mathrm{Re} \leq 600$.

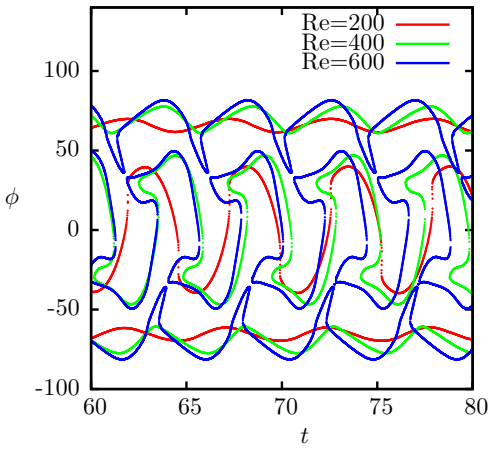

Figure 11: P2-P4 separation positions for $\tilde{T} = 1.5$.

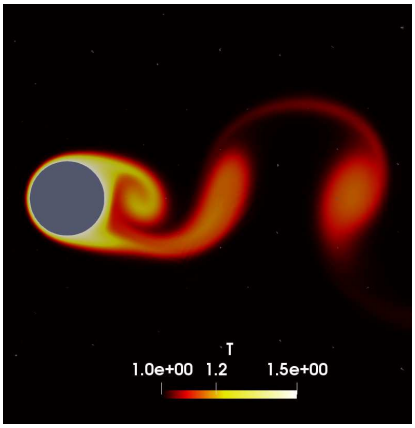

Figure 12: Temperature field, $\tilde{T} = 1.5$, Re = 600.

With further increase in Re curves P2 and P3 become closer to P4 (Re = 500 in Figure 10) and separations emerge in all these positions. However, for Re = 600 curves P2, P3 and P4 merge to a single curve and separations emerge only in range of former positions P2 and P3. Critical Reynolds number for this transition seems to be close to Re = 500. Between Re = 600 and Re = 800 another transition exists. The single curve again separates, but closed curves are observed in former ranges of P2 and P3. The closed curves indicate, that vortices are shedding directly from the surface and do not merge with other vortices directly on the surface (merging is possible downstream).

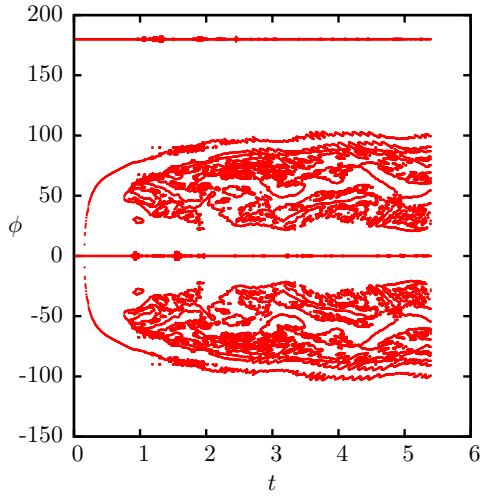

Figure 13: Detected separations on cylinder Re = 20000.

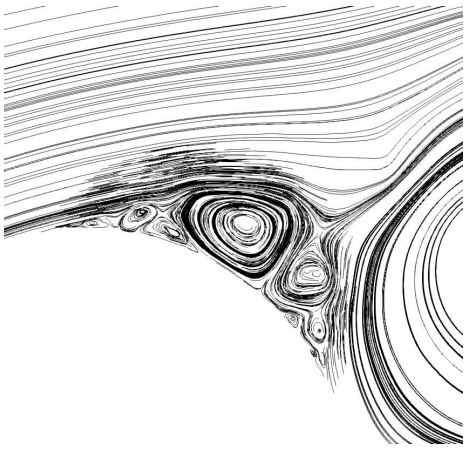

Figure 14: Streamlines in boundary layer area, Re = 20000.

For higher Re, all the curves are getting more complex shapes as separation points emerge at new positions. Detail description of these complicated structures is beyond the scope of this contribution. We only show result for Re = 20000, the highest Re used in our study, computed on high order quadrilateral mesh with polynomial degree $N = 24$, see Figure 13. Curve patterns

become so complicated that statistical consideration should be done rather than description of particular separations and vortex formations. In this case, we observe a kind of symmetry around $\phi = 0$ and region $-20 \lesssim \phi \lesssim 20$ to be clean of separations. Despite of very strong spatial approximation, we can see rare but spurious detections of separations around angles, where are element corners, what indicates very steep velocity gradients in the boundary layer.

5 Conclusion

Analysis of flow separation points over the cylinder surface clearly shows qualitative changes in structure of vortex formation for both the isothermal and heated surface.

Generally, it was observed in present simulations, that separation points emerge and disappear in pairs and that *a point of separation, once emerged, do not disappear alone*.

There were many substantial changes in flow patterns observed, some of them well coinciding with already described phenomenons, but others are trusted to be new. For every change between flow patterns, we can define a critical Re, but this work only sketched the new approach of analysis of separation points detection, while accurate determination of these critical Reynolds numbers is left for future work.

Results concerning the heated case confirmed expectation, that the air flow patterns are similar to those with lower Re isothermal flow.

A large number of computations was devoted to testing parameters of the numerical method, but a lot of possibilities for optimizations still exist as is evident from sensitive analysis of expansion coefficients spectra, a tool for estimates of spatial error in the numerical approximation.

This work showed only chosen results from application of the separation points analysis and the newly developed spectral/hp solver for the Navier-Stokes-Fourier system, while wider range of Re and $\tilde{T}$ was already studied, but is beyond the scope of this paper.

Acknowledgment

The author wishes to acknowledge the support of the Czech Academy of Sciences, project MSM100761901.

References

[1] C. Cantwell et al. Nektar++: An open-source spectral/hp element framework. *Computer Physics Communications*, 192:205 – 219, 2015.

[2] M. Coutanceau and J.-R. Defaye. Circular Cylinder Wake Configurations: A Flow Visualization Survey. *Applied Mechanics Reviews*, 44(6):255–305, 06 1991.

[3] G. Karniadakis and S. Sherwin. *Spectral/hp Element Methods for Computational Fluid Dynamics: Second Edition*. Numerical Mathematics and Scientific Computation. Oxford, 2005.

[4] G. E. Karniadakis, S. A. Orszag, and M. Israeli. High-order splitting methods for the incompressible Navier-Stokes equations. *Journal of Computational Physics*, 97:414–443, Dec. 1991.

[5] J. Pech. Scheme for evolutionary Navier-Stokes-Fourier system with temperature dependent material properties based on spectral/hp elements. In *Lect. Notes Comput. Sci. Eng.*, In print.

[6] J. Pech and P. Louda. Comparison of finite volume and spectral/hp methods on navier - stokes equations for unsteady incompressible flow. In *Proceedings Topical Problems of Fluid Mechanics 2018*, pages 223–230, 2018.

[7] A.-B. Wang and Z. Trávníček. On the linear heat transfer correlation of a heated circular cylinder in laminar crossflow using a new representative temperature concept. *International Journal of Heat and Mass Transfer*, 44(24):4635 – 4647, 2001.

[8] A.-B. Wang, Z. Trávníček, and K.-C. Chia. On the relationship of effective Reynolds number and Strouhal number for the laminar vortex shedding of a heated circular cylinder. *Physics of Fluids*, 12(6):1401–1410, 2000.